

http://pubs.acs.org/journal/aelccp

Onset of Lithium Plating in Fast-Charging Lilon Batteries

Weiyu Li*



Cite This: ACS Energy Lett. 2025, 10, 1596-1604



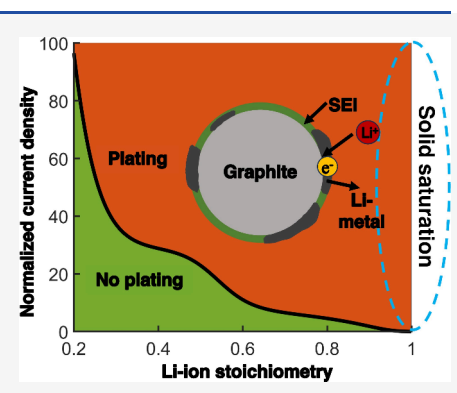
ACCESS I

Metrics & More

Article Recommendations

Supporting Information

ABSTRACT: Lithium (Li) plating is a major challenge limiting the adoption of fast-charging Li-ion batteries, yet its onset mechanisms remain elusive. We present a model of Li plating on a graphite particle coated with a solid electrolyte interphase (SEI) layer to elucidate the coupled effects of ion transport, reaction kinetics, and phase transformation. We derive an analytical expression that relates Li-plating onset time to operating conditions and material properties and introduce a Li-plating diagram. Our framework captures the intricate mechanisms driving Li plating and anode potential drops, extending beyond existing limiting cases of surface ion saturation and electrolyte depletion. By providing an improved understanding of the interrelationships among key parameters, our findings provide valuable guidance for adjusting charging protocols, designing cell components, and engineering artificial SEI layers. Implementing these strategies can help mitigate Li plating and ensure Li-ion battery safety and performance during fast charging.



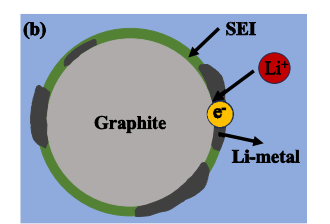
ithium (Li) plating is one of the major challenges that impedes the widespread adoption of rapid charging for Li-ion batteries. Critical issues arise when Li plating occurs, including capacity fading, poor cyclability, reduced reversibility and increased internal resistance, jeopardizing batteries' operational safety and structrural integrity. Interfacial instability associated with Li-metal deposition results in the formation of Li dendrite, causing catastrophic failures in Li-ion batteries. Understanding the mechanisms of Li plating onset is essential to ensuring the safety and stable performance of Li-ion batteries during fast charging.

During charging, Li-ions (Li⁺) migrate from the liquid electrolyte and intercalate into the graphite anode. Multiple physical and electrochemical processes, including liquid and solid diffusion, electromigration and charge transfer reactions, lead to variations in ion concentration and electric potential profiles, as well as changes in overpotential at the electrode/ electrolyte interfaces. A further drop in anode potential, especially under fast charging conditions, can make Li plating thermodynamically favorable when the Li-plating overpotential falls below zero. Experimental efforts to prevent Li plating include design and optimizing various cell components, such as coating graphite with solid electrolytes, metals or functional promoters, fo electrolyte engineering such as using localized high-concentration electrolyte, 12 and incorporating additives, 13,14 and implementing anode potential-controlled charging protocols. 15 These experimental investigations can greatly benefit from physics-based electrochemical modeling. Such models provide quantitative predictions of Li⁺ transport and electrochemical reactions within each battery component, offering valuable insights to refine strategies to mitigate Li plating.

Modeling work on this subject is typically conducted at two extremes: density functional theory (DFT) and pseudo-twodimensional (P2D) models. DFT provides atomic-scale insights into diffusion pathways, formation energies, and phase transitions influencing plating, 16-19 but its computational demands make it impractical for resolving pore-scale electrochemical interactions at electrode/electrolyte interfaces. 20,21 On the other hand, the computationally efficient P2D models treat porous electrodes as one-dimensional (1D) continuum media, limiting their ability to capture the in-depth mechanisms of plating onset and transport phenomena. 22 Moreover, P2D models lose predictive accuracy under high current conditions where plating is more pronounced. ^{23,24} The ubiquitous presence of an interface layer, such as the solid-electrolyte interphase (SEI) or artificial coating layer, adds further complexities. Previous studies have incorporated SEI film resistance into Butler–Volmer kinetics at the anode/electrolyte interface, ^{25–27} though SEI is not purely an ohmic resistor. 28 The detailed effects of mass and charge transport within SEI, governed by its specific

Received: January 29, 2025 Accepted: February 28, 2025





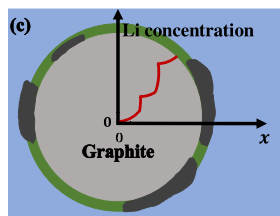


Figure 1. (a) Schematic representation of the 1D computational domain considered in this study. Our model consists of an anode particle $\Omega_{\rm a}$ and a cathode particle $\Omega_{\rm c}$ that are immersed in liquid electrolyte $\Omega_{\rm e}$ within a Li-ion battery. We account for Li⁺ diffusion, electromigration, ion intercalation/deintercalation and Li plating kinetics in the 1D computational domain. (b) Li-metal is deposited on the graphite surface when the Li-plating overpotential, $\eta_{\rm pl} = \phi_{\rm a}(L_{\rm a},t) - \phi_{\rm e}(L_{\rm a},t)$ drops below zero. (c) Illustration of Li concentration profile in the graphite particle with phase separation.

physicochemical properties, are critical yet remain largely unexplored in the context of plating. ^{29,30} Moreover, phase transformation and separation occur during Li (de)intercalation in electrode materials such as graphite and lithium iron phosphate, causing uneven Li distribution and impacting the availability of Li intercalation sites in the electrodes. ^{31,32} These effects become more pronounced during fast charging. ^{33,34} The coupling of these phenomena introduces additional complexities and computational cost to resolve the Li⁺ concentration profiles in the solid particles. ^{35,36}

These challenges have led existing studies to attribute the mechanisms of plating onset to ion concentration saturation at the intercalation-host surface, ^{36,37} ion depletion in the electrolyte at the solid/liquid interface, ^{38–40} or large ion concentration gradients at the solid surface. ⁴¹ However, plating initiates even at very low states of charge before ion concentration at the solid surface saturates ⁴² or at current densities significantly below their limiting value. ³⁶ This suggests that plating results from a complex interplay among multiple physical and electrochemical processes rather than being governed by a single limiting factor. Currently, a comprehensive theoretical framework of plating mechanisms that accounts for these complexities is lacking.

We fill this void by presenting a mesoscale model for Li plating on a graphite particle coated with an SEI layer. The model incorporates ion diffusion and electromigration, as well as the competition between ion intercalation and Li plating kinetics. Our analysis generalizes the conditions for Li plating beyond previously reported limiting cases. We derive an analytical expression that relates the onset time of Li plating to measurable characteristics, such as current density and material properties, enabling a Li-plating diagram that delineates plating conditions. These results offer valuable insights for delaying or even preventing Li plating through adjustments to charging protocols and the design and selection of cell components. Such decisions should be informed by the material properties and Li+ stoichiometry. While applied to Li plating, this model has broader relevance for understanding metal plating in various electrochemical systems.

We study Li plating on a graphite anode in a Li-ion battery. Our model consists of an anode particle $\Omega_{\rm a}$ and a cathode particle $\Omega_{\rm c}$ that are immersed in liquid electrolyte $\Omega_{\rm e}$ (Figure 1a). Past experimental works indicate that Li plating predominantly initiates at the anode/separator interface. Multiparticle modeling confirms this interface as the primary site for plating initiation. This study focuses on single particles at the anode/separator interface to capture the key mechanisms driving Li plating onset, consistent with literature that emphasizes the critical role of this region. We ignore convective ion transport in the electrolyte and assume the

electrolyte to be electroneutral, where the concentrations of cations, $c_+(x, t)$ and anions, $c_-(x, t)$, are equal, i.e., $c_+ = c_- = c_e$. Mass conservation of Li⁺ in the electrolyte is described by the Nernst–Planck equation,

$$\frac{\partial c_{\rm e}}{\partial t} = -\frac{\partial J_{+}}{\partial x}, L_{\rm a} \le x \le 2L - L_{\rm a}, t > 0 \tag{1a}$$

Mass fluxes of cations, $J_+(x, t)$, and anions, $J_-(x, t)$ are induced by the spatial variability of ion concentration $c_e(x, t)$ and electric potential $\phi_e(x, t)$,⁷

$$J_{\pm} = -D_{\pm} \left(\frac{\partial c_{\rm e}}{\partial x} + \frac{z_{\pm} c_{\rm e} F}{RT} \frac{\partial \phi_{\rm e}}{\partial x} \right) \tag{1b}$$

where D_{\pm} and z_{\pm} are the diffusion coefficients and charge numbers of the cations and anions; F is the Faraday constant. The charge conservation equation is given by

$$\frac{\partial \mathcal{J}}{\partial x} = 0, L_{a} < x < 2L - L_{a}, t > 0$$
(2)

where $\mathcal{J}=z_+FJ_++z_-FJ_-$ is the electrolyte current density. Equations (1) and (2) are subject to the boundary conditions, $-J_+(L_a, t) = J_+(2L - L_a, t) = I/F, -\mathcal{J}(L_a, t) = \mathcal{J}(2L - L_a, t) = I$ and initial condition, $c_e(x, 0) = c_0$, where I is the applied constant charging current density.

At the anode/electrolyte interface, Li^+ are inserted into the graphite particle through intercalation reactions with electrons (e^-) , $C_6 + n \text{Li}^+ + n e^- \rightarrow \text{Li}_n C_6$, while Li^+ are deintercalated from the cathode into the liquid electrolyte. The intercalation reactions are described by the Butler–Volmer (BV) equations,

$$I_{i,\text{int}} = -2k_{i,\text{int}}F\sqrt{c_ic_e(1-c_i/c_{i,\text{max}})}$$

$$\times \sinh\left[\frac{F}{2RT}(\phi_i - \phi_e - U_i(c_i/c_{i,\text{max}}))\right]$$
(3)

here, i=a, c denotes the index representing anode and cathode quantities. U_i is the open circuit potential that depends on the Li filling fraction $c_i/c_{i,\text{max}}$; $k_{i,\text{int}}$ is the reaction rate constant and $c_{i,\text{max}}$ is the maximum Li concentration that could be stored in the particles. At x=L, we set $\phi_e=0$. Li plating becomes thermodynamically favorable when the Li-plating overpotential $(\eta_{\text{pl}}=\phi_a-\phi_e-\Delta\phi_{\text{eq,pl}})$ drops below zero. This negative potential drives Li⁺ to undergo Faradaic reactions with e^- , Li⁺ + $e^- \to \text{Li}$, which results in Li plating on the graphite surface (Figure 1b). The plating kinetics also follows a BV equation, 49,50

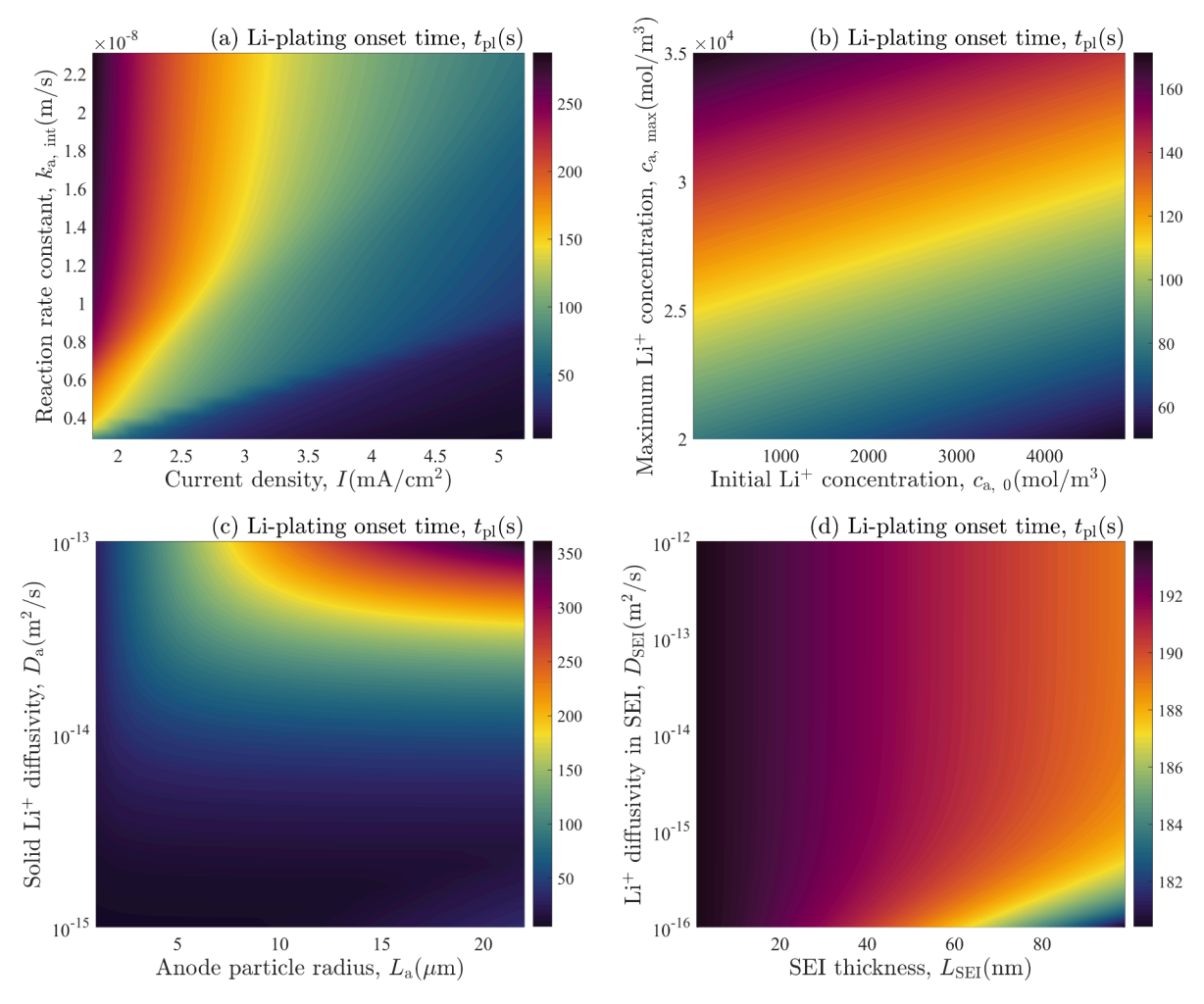


Figure 2. Li-plating onset time t_{pl} computed by eq 8, varies with (a) current density I and intercalation rate constant $k_{a,int}$ (b) initial and maximum Li^+ concentrations in the anode, $c_{a,0}$ and $c_{a,max}$ (c) particle size L_a and Li^+ diffusivity D_a , (d) SEI layer thickness L_{SEI} and diffusion coefficient D_{SEI} . In each plot, all parameters, except for the ones under investigation, are set to their reference values as specified in Table S1, and $L_{SEI} = 0$ when SEI properties are not explored in a-c.

$$I_{\rm pl} = -k_{\rm pl}F(c_{\rm e}/c^{\Theta})^{\alpha_{\rm an}} \times \left[\exp\left(\alpha_{\rm an}\frac{F\eta_{\rm pl}}{RT}\right) - \exp\left(-\alpha_{\rm cat}\frac{F\eta_{\rm pl}}{RT}\right)\right]$$
(4)

where $k_{\rm pl}$ is the plating reaction rate constant; $\alpha_{\rm an}$ and $\alpha_{\rm cat}$ are the anodic and cathodic charge-transfer coefficients, respectively; $\Delta\phi_{\rm eq,pl}$ is the equilibrium potential of Li plating reaction given by the Nernst equation,

$$\Delta \phi_{\text{eq,pl}} = \frac{RT}{F} \ln \frac{c_{\text{e}}(L_{\text{a}}, t)}{c^{\Theta}} + E^{\Theta} - \frac{2\omega\gamma\kappa}{F}$$
 (5)

where we account for the influence of electrode/electrolyte interfacial energy, $2\omega\gamma\kappa/F$, since the creation of additional surface area results in a surface energy penalty. ω and γ are the molar volume and surface energy of Li metal; κ is the curvature of the electrode/electrolyte interface, $\kappa = 1/L_{\rm a}$. $I_{i,\rm int}$ and $I_{\rm pl}$ are related to the total current density $I_{i,\rm pl}$

$$I_{\text{a,int}} + pI_{\text{pl}} = I, x = L_{\text{a}}$$
 (6a)

$$I_{c,int} = -I, x = 2L - 2L_a$$
 (6b)

p = 0 indicates that only ion intercalation occurs at the anode, while p = 1 signifies the occurrence of Li plating.

With azimuth and polar symmetry in spherical coordinates, ion concentration $c_i(r, t)$ in the electrode particles is described by the diffusion equations, ⁵¹

$$\frac{\partial c_i}{\partial t} = \frac{1}{r^2} \frac{\partial}{\partial r} \left(D_i r^2 \frac{\partial c_i}{\partial r} \right), \quad 0 < r < L_i, \quad t > 0$$
(7)

where D_i is the solid diffusion coefficient. Equation 7 is subject to the boundary conditions, $D_{\rm a} \frac{\partial c_a}{\partial r} (r=L_a,\,t) = -D_{\rm c} \frac{\partial c_c}{\partial r} (r=L_c,\,t) = \frac{I}{F},\, D_{\rm a} \frac{\partial c_a}{\partial r} (r=0,\,t) = -D_{\rm c} \frac{\partial c_c}{\partial r} (r=0,\,t) = 0$ and initial condition, $c_i(r,0) = c_{i,0}$. We also neglect the effects of solid particle volume changes, stress generation, and dynamic SEI layer growth. We assume the SEI is fully formed and characterized by predefined Li⁺ diffusion coefficient $D_{\rm SEI}$ (Figure 1b). The SEI influences ionic transport by modifying key parameters, $D_{\rm a},\,c_{\rm a,0},\,c_{\rm a,max}$ and $k_{\rm a,int}$, as functions of the graphite core volume fraction and transport properties of the graphite core and SEI, given in Appendix B.

From eqs 1–7, we derive an analytical expression of plating onset time, $\tilde{t}_{\rm pb}$ with the detailed derivation provided in Appendix B.

$$\left(\frac{\tilde{I}e^{-Ca}}{\tilde{k}_{a,int}\sqrt{\tilde{c}^{\Theta}}}\right)^{2}\frac{1}{\tilde{c}_{a,max}} = f[\tilde{c}_{a}(\tilde{L}_{a}, \tilde{t}_{pl})/\tilde{c}_{a,max}]$$
(8)

as a function of dimensionless quantities, $\tilde{x} = x/L$, $\tilde{t} = tD_+^{\rm ref}/L^2$, $\tilde{c} = c/c_0$, and model parameters $\tilde{D} = D/D_+^{\rm ref}$, $\tilde{k} = Lk/D_+^{\rm ref}$, capillary number Ca = $\omega\gamma/(RTL_{\rm a})$, normalized interfacial current density $\tilde{I} = LI/(D_+^{\rm ref}Fc_0)$ and open circuit potential $\tilde{U} = FU/(RT)$; where f is a function of the Li⁺ stoichiometry, $\xi = \tilde{c}_{\rm a}(\tilde{L}_{\rm a}, \tilde{t}_{\rm pl})/\tilde{c}_{\rm a,max}$, in the anode,

$$f(\xi) = \xi(1 - \xi)e^{\tilde{U}_{a}(\xi)} \tag{9}$$

and $\tilde{c}_a(\tilde{L}_a,\tilde{t})$ approximates the large-time ion concentration at the anode surface,

$$\tilde{c}_{a}(\tilde{L}_{a}, \tilde{t}) = \frac{3\tilde{I}}{\tilde{L}_{a}}\tilde{t} + \frac{\tilde{I}\tilde{L}_{a}}{5\tilde{D}_{a}} + \tilde{c}_{a,0}$$
(10)

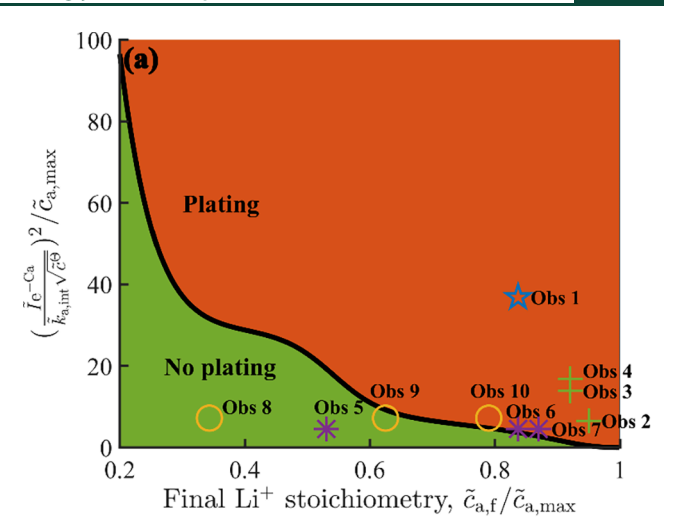
Figure 2 illustrates the Li-plating onset time $t_{\rm pl}$, calculated by eq 8. We investigate the impact of various parameters, including current density I, intercalation rate constant $k_{a,int}$ initial and maximum Li^+ concentrations, $c_{a,0}$ and $c_{a,max}$, particle size L_a , Li^+ diffusivity D_{a} , SEI layer thickness $L_{\rm SEI}$ and diffusion coefficient $D_{\rm SEI}$. In each plot, all parameters, except for the ones under investigation, are set to their reference values as specified in Table S1, and $L_{SEI} = 0$ when SEI properties are not under investigation. A small current density or a large intercalation rate constant, a small initial Li⁺ concentration, a large maximum Li⁺ concentration or a large Li⁺ diffusivity in the anode particle, a thin SEI layer with high Li⁺ diffusivity, will delay the onset of Liplating. Our analytical expression also shows that the surface energy term, e^{-Ca}, has negligible impact on Li plating despite its critical role in affecting dendrite growth. 7,50 The bulk ion concentration c_0 does not impact Li-plating onset. However, an electrolyte with a higher salt concentration may result in the formation of a thinner and more compact SEI layer, 52-54 influencing plating dynamics. These findings can provide valuable insights into the design of artificial SEI layers with specific thickness and Li⁺ diffusion coefficients to effectively delay the occurrence of Li-plating.

Next, we include the impact of phase transformation and separation during Li (de)intercalation in electrode particles (Figure 1c). This can be described with a variable solid diffusion coefficient 35,55,56 in eq 7, i.e.,

$$\mathcal{D}_{i}(c_{i}) = -(1 - \theta)\theta D_{i}' \frac{d\tilde{U}(\theta)}{d\theta}$$
(11)

where $\theta = c_i/c_{i,max}$. The resulting concentration profiles are similar to the solutions of the corresponding moving boundary problem for phase transition. The analytical solution of large-time ion concentration at the anode surface given in eq 10 holds by treating the concentration-dependent diffusion coefficients as piece-wise constants. The resulting concentration of the concentration of the surface given in eq 10 holds by treating the concentration of the surface given in eq 10 holds by treating the concentration of the corresponding moving boundary problem for phase transition.

A Li-plating diagram is shown in Figure 3a in the phase space spanned by dimensionless parameters, current density \tilde{I} , reaction constant $\tilde{k}_{\text{a,int}}$ capillary number Ca, maximum Li⁺ concentration $\tilde{c}_{\text{a,max}}$ Li⁺ concentration at the solid surface $\tilde{c}_{\text{a,f}}$ and reference concentration \tilde{c}^{Θ} . This is governed by the condition under which no Li plating occurs,



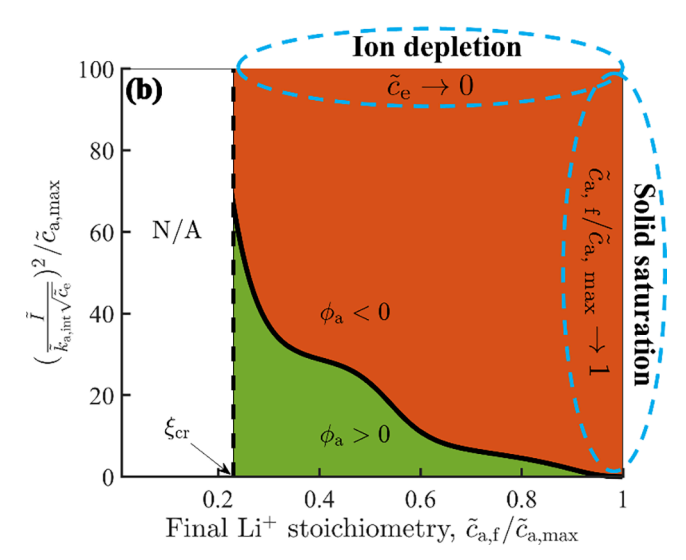


Figure 3. (a) Li-plating and (b) anode potential diagrams in the phase space spanned by dimensionless current density I, reaction constant $\tilde{k}_{a,int}$ capillary number Ca, maximum Li⁺ concentration $\tilde{c}_{a,\max}$, Li⁺ concentration at the solid surface $\tilde{c}_{a,f}$, reference concentration \tilde{c}^{Θ} , and electrolyte Li⁺ concentration at the liquid/ solid interface \tilde{c}_e , described by eqs 12 and 13. The solid line in (a) separates the non-plating and plating regions, while in (b), it separates the positive and negative anode potential regions, such that for given operating conditions and material's physical and electrochemical properties, the Li-plating overpotential $\eta_{\rm pl}$ or the anode potential ϕ_a is predicted to either drop below zero (red region to the right of the solid line) or remain positive (green region to the left of the solid line). In (b), the dashed line denotes the critical value of Li⁺ stoichiometry in the anode, ξ_{cr} , defined by (B15), to the right of which this diagram is applicable. In (a), the Li-plating diagram is compared with experimental data from refs 2 and 58-60. Details of the experimental conditions and parameters are provided in Supporting Information Table S2. In (b), surface Li⁺ saturation $(\tilde{c}_{a,f}/\tilde{c}_{a,max} \rightarrow 1)$ and liquid Li⁺ depletion at the anode/electrolyte interface $(\tilde{c}_e \rightarrow 0)$ are two limiting cases that lead to a negative anode potential.

$$\left(\frac{\tilde{I}e^{-Ca}}{\tilde{k}_{a,int}\sqrt{\tilde{c}^{\Theta}}}\right)^{2}\frac{1}{\tilde{c}_{a,max}} < f(\xi_{f})$$
(12)

where $\xi_f = \tilde{c}_{a,f}/\tilde{c}_{a,max}$ represents the final Li⁺ stoichiometry at the anode particle surface. The solid line separates the non-plating

and plating regions such that for given operating conditions and material's physical and electrochemical properties, the Li-plating overpotential $\eta_{\rm pl}$ is predicted to either drop below zero (red region to the right of the solid line) or remain positive (green region to the left of the solid line). For a given final Li⁺ stoichiometry, plating is more likely to occur under fast charging conditions or when the Li intercalation rate constant or maximum Li⁺ concentration is small. This Li-plating diagram provides an improved understanding of the interrelationships among key parameters and identifies specific operating conditions that prevent Li plating. We validate our plating diagram against experimental data. This process proved to be challenging due to the frequent reporting of charging conditions in terms of C-rate rather than current density and the lack of detailed material properties in many experiments. We compiled experimental data that included the necessary parameters and real-time plating detection from refs 2, 58-60. A detailed summary of the operating conditions and parameters for these experiments is provided in Information Table S2. All experimental results available to us align with the predictions of our plating diagram. Specifically, data points 6 and 9 that represent conditions leading to plating onset in the experiments^{59,60} are located close to the boundary separating the plating and non-plating regions. This further confirms the diagram's predictive accuracy in capturing the onset of Li plating under various conditions. Figure 3b presents the anode potential diagram in the phase space spanned by dimensionless parameters, as described by

$$\left(\frac{\tilde{I}}{\tilde{k}_{a,\text{int}}\sqrt{\tilde{c}_{e}}}\right)^{2} \frac{1}{\tilde{c}_{a,\text{max}}} < f(\xi_{f})$$
(13)

which ensures that the anode electric potential remains positive. The detailed derivation is provided in Appendix B. \tilde{c}_e is the steady-state Li⁺ concentration in the electrolyte given by eq B2 at $\tilde{x} = L_a/L$. The dashed line represents the critical value of Li⁺ stoichiometry in the anode, defined by eq B15, to the right of which the characteristic diffusion time of Li⁺ in the liquid electrolyte is smaller than the final charging time, rendering this diagram applicable. Our anode potential diagram aligns with previous studies under scenarios where the surface Li concentration in the anode particle saturates $(\tilde{c}_{a,f}/\tilde{c}_{a,max} \rightarrow$ 1)^{36,37} or when Li⁺ are depleted at the anode/electrolyte interface $(\tilde{c}_e \rightarrow 0)$. These limiting cases of negative anode potential coincide with our diagram's predictions, falling within the red region where the anode potential drops below zero. The anode potential diagram differs from the plating diagram in that it relies on ion transport in the liquid electrolyte. As c_e is smaller than the bulk ion concentration, there exists a region where data points fall within the range where the anode potential becomes negative while remaining in the non-plating regime. We can calculate the time at which the anode potential drops to zero $t_{\phi_a<0}$ by eq B11, and find that it occurs earlier than the plating onset time $t_{\rm pl}$. This phenomenon arises from the combined effects of negative electrolyte potential and concentration overpotential at the anode/electrolyte interface (eq 5). This finding is consistent with prior studies in the literature indicating that graphite can sustain a small negative potential before plating occurs. 61,62

We also carry out numerical simulations to capture the details of electric potential and ion concentration profiles and temporal evolution of plating overpotential. These simulations consider the influence of applied current densities, diffusion coefficients, and intercalation and plating rate constants on ion transport and reaction kinetics. The materials and parameter values used in our model and the numerical results are provided in Supporting Information. Specifically, in Figure 4, we compare the temporal

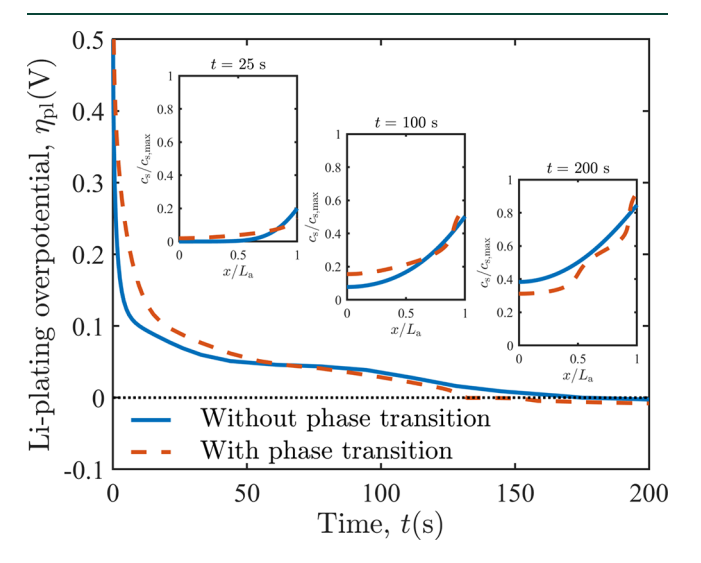


Figure 4. Temporal evolutions of Li-plating overpotential $\eta_{\rm pl}$ at the anode surface $(x=L_{\rm a})$ under scenarios with and without phase transformation in the graphite particle at a constant current density of $I=3~{\rm mA/cm^2}$. Snapshots of Li⁺ concentration profiles within the graphite particle show that including phase transformation results in sharper concentration gradients and higher Li⁺ content at the graphite surface, leading to earlier plating onset.

evolution of Li-plating overpotential (η_{pl}) on the anode surface $(x = L_a)$ under scenarios with and without phase transformation by using constant and variable diffusion coefficients in the graphite particle at a constant current density of $I = 3 \text{ mA/cm}^2$. For consistency, diffusion coefficient D'_a in eq 11 is chosen such that $\int_0^1 \mathcal{D}_i(c_i) d\theta = D_a$ matching the constant value specified in the Supporting Information Table S1. We also present snapshots of Li⁺ concentration distributions in the graphite particle over time. When phase transformation is included, the concentration profiles at later stages show pronounced sharp changes, with phase separation leading to a higher Li⁺ concentration at the graphite surface. This behavior accelerates the onset of Li plating compared to models that use a constant diffusion coefficient and exclude the phase transition effects. In this example, neglecting phase transformation phenomena results in ~35% delay in the predicted time for Li-plating occurrence. Our results highlight the critical role of phase transformation in accurately predicting plating onset.

Our findings reveal the mechanisms behind anode potential drops and their potential connection to Li plating. A negative anode potential is not solely a result of Li⁺ surface saturation in the solid particle or Li⁺ depletion at the anode/electrolyte interface, as commonly assumed. Instead, it can arise before the solid surface ion concentration saturates or the applied current density exceeds the limiting value that leads to Li⁺ depletion. This phenomenon results from a complex interplay between solid and liquid diffusion, electromigration, intercalation, and plating kinetics. First, slow solid diffusion or high current density creates a high concentration gradient near the anode particle surface, impeding ion diffusion from the surface to the interior.

Second, the presence of a high surface concentration of Li⁺ in the anode particle, a low electrolyte Li⁺ concentration at the anode/ electrolyte interface, or a small intercalation reaction rate constant makes Li intercalation into the anode particle kinetically challenging. The occurrence of phase transition and phase separation within the anode particle further amplifies the Li⁺ concentration and its gradient near the particle surface, exacerbating these effects. Third, the formation of SEI layer with low solid diffusion coefficient hampers ion diffusion and introduces interfacial charge resistance. These factors collectively impact the availability of Li+ in the liquid electrolyte and the occupation of intercalation sites in the solid particle, creating barriers for charge transfer reactions. To maintain current density, the negative intercalation overpotential must further decrease. Additionally, the anode intercalation equilibrium potential decreases as Li⁺ intercalates into the particle, and the electrolyte potential at the anode/electrolyte interface reduces under high current density or small diffusion coefficient in the liquid electrolyte. These combined effects lead to a drop in the anode potential. However, a negative anode potential may indicate conditions favorable to Li plating but it is not equivalent to its occurrence. 60 This distinction stems from the independence of Li-plating overpotential, $\eta_{\rm pl} = \phi_{\rm a}(L_{\rm a},\ t)$ $\phi_{\rm e}(L_{\rm a},t) - \Delta\phi_{\rm eq,pl}$ from ion transport in the liquid electrolyte. The effect of local concentration on altering the anode potential is counteracted by the concentration overpotential, $rac{RT}{F} {
m ln} \; c_e(L_a, \, t)/c^\Theta$ The often reported link between Li plating and ion depletion $^{38-40}$ can be attributed to the fact that plating typically occurs before ion depletion, e.g., the saturation of graphite surface $(\tilde{c}_{a,f}/\tilde{c}_{a,max} \rightarrow 1)$ proceeds the Li⁺ depletion $(\tilde{c}_e \rightarrow 0)$ in the electrolyte. Currently, no experimental data exist in the opposite regime, where ion depletion occurs while the solid surface concentration remains low. Our insights provide a foundation for future experimental investigations of Li plating in this regime, which will aid in further understanding plating mechanisms and validating our theory.

In conclusion, we developed a mechanistic model for Li plating on a graphite particle coated with an SEI layer in a Li-ion battery. This model accounts for ion transport, reaction kinetics, and phase transformation phenomena, exploring the complex interplay of these processes and their effects on the onset of Li plating. Our analytical framework generalizes the conditions for Li plating and introduces plating and anode potential diagrams that offer insights into the key factors driving anode potential changes and plating initiation. Our analysis leads to the following major conclusions.

- Our plating diagram captures the onset of Li plating under various operating conditions and material properties in the experiments. The simplicity of this diagram assists in designing charging protocols, e.g., decreasing current density as state-of-charge increases.
- Our analysis shows that Li plating is more likely to occur
 under fast-charging conditions, or with a small intercalation rate constant, large solid surface concentration,
 low maximum Li⁺ concentration and low Li⁺ diffusivity in
 the anode particle, or with an SEI layer that has low Li⁺
 diffusivity. The presence of phase transformation and
 separation further exacerbates Li plating. Surface energy
 has a negligible effect on the onset of Li plating.
- Our results clarify that the onset of a negative anode potential does not signal plating initiation, as is commonly assumed. The anode can sustain a negative potential

- before plating occurs. Our analysis shows that changes in anode potential are influenced by ion transport in the liquid electrolyte, while the Li-plating overpotential is independent of ion transport in the electrolyte.
- Surface saturation is the limiting case that leads to Li plating. Surface saturation and electrolyte depletion are the two limiting cases that lead to negative anode potential. Our theory reflects the intricate and coupled mechanisms underlying Li plating and anode potential drops beyond these specific instances.

These findings provide practical guidelines for optimizing charging protocols, cell design, and interface engineering. This work lays the foundation for future studies aimed at enhancing the performance and safety of fast-charging Li-ion batteries through physics-based design principles.

APPENDIX A

SEI Effects

We consider the anode particle as a composite sphere whose active material (graphite) core is coated with an SEI layer. We model this composite sphere as a homogeneous anode particle with derived physicochemical properties that ensure the global conservation of mass, energy, and charge. Here, SEI layer impacts the overall ionic transport in this anode particle by altering the Li⁺ diffusion coefficient $D_{\rm av}$ initial and maximum Li concentrations $c_{\rm a,0}$ and $c_{\rm a,max}$, and reaction rate constant $k_{\rm a,int}$. They are expressed in terms of the volume fraction of the graphite core and transport properties of the graphite core and SEI^{24,51}

$$D_{a} = \left\{ 5 \frac{1 - V_{1}}{D_{SEI}} \left[\frac{(1 - V_{1}^{1/3})^{2} + 3(V_{1}^{1/3} + 2)(1 - V_{1}^{1/3})}{2(1 - V_{1}^{1/3})^{2} + 6V_{1}^{1/3}} - \frac{3(1 - V_{1}^{1/3})^{2}}{1 - V_{1}} \right] + \frac{V_{1}^{2/3}}{D_{gr}} \right\}^{-1}$$
(A1a)

$$c_{a,max} = c_{gr,max} V_1, c_{a,0} = c_{gr,0} V_1$$
 (A1b)

and

$$k_{\text{a,int}} = k_{\text{gr,int}} V_1^{7/6} \sqrt{\frac{1 + 2V_1^{1/3}}{7 + 2V_1^{1/3}}}$$
 (A1c)

where V_1 is the volume fraction of graphite active material in the composite anode, i.e., $V_1 = (L_{\rm a} - L_{\rm SEI})^3 / L_{\rm a}^3; \ D_{\rm gr}, \ c_{\rm gr,max}, \ c_{\rm gr,0}$ and $k_{\rm gr,int}$ are the Li ion diffusion coefficient, maximum and initial Li concentrations, and reaction rate constant in the graphite particle; $D_{\rm SEI}$ is the Li⁺ diffusivity in the SEI layer.

APPENDIX B

Plating Onset Conditions

We introduce dimensionless variables

$$\tilde{x} = \frac{x}{L}, \, \tilde{t} = \frac{tD_{+}^{\text{ref}}}{L^2}, \, \tilde{c} = \frac{c}{c_0}, \, \tilde{\phi} = \frac{F\phi}{RT}, \, \tilde{\eta} = \frac{F\eta}{RT}$$
 (B1a)

and model parameters

$$\tilde{D} = \frac{D}{D_{+}^{\text{ref}}}, \, \tilde{c}^{\Theta} = \frac{c^{\Theta}}{c_{0}}, \, \tilde{k} = \frac{Lk}{D_{+}^{\text{ref}}}$$
(B1b)

We also define the capillary number

$$Ca = \frac{\omega \gamma}{RTL_a}$$
 (B1c)

and the normalized interfacial current density \tilde{I} and open circuit potential \tilde{U} as

$$\tilde{I} = \frac{LI}{D_{+}^{\text{ref}}Fc_0}, \ \tilde{U} = \frac{FU}{RT}$$
(B1d)

Unless specified otherwise, all the quantities below are dimensionless, even though we drop the tildes to simplify the notation.

The steady-state Li⁺ concentration c_e and electric potential ϕ_e in the liquid electrolyte at the final charging times can be solved analytically,

$$c_{\rm e}(x) = \frac{I}{2D_{+}}(x-1) + 1, \, \phi_{\rm e} = \ln c_{\rm e}$$
 (B2)

Prior to the onset of plating, the ion concentration inside the anode particle with a constant diffusion coefficient $D_{\rm a}$ can be determined using Laplace transform, ⁵¹

$$c_{\mathbf{a}}(r,t) = \mathcal{L}_{\lambda}^{-1} \left[\frac{IL_{\mathbf{a}}^{2}}{D_{\mathbf{a}}r\lambda} \alpha (\mathbf{e}^{r\sqrt{\lambda/D_{\mathbf{a}}}} - \mathbf{e}^{-r\sqrt{\lambda/D_{\mathbf{a}}}}) + \frac{c_{\mathbf{a},0}}{\lambda} \right]$$
(B3a)

where λ is the Laplace-transform variable and \mathcal{L}_T^{-1} denotes inverse Laplace-transform and

$$\alpha = \frac{1}{(L_{\rm a}\sqrt{\lambda/D_{\rm a}} + 1)e^{-L_{\rm a}\sqrt{\lambda/D_{\rm a}}} + (L_{\rm a}\sqrt{\lambda/D_{\rm a}} - 1)e^{L_{\rm a}\sqrt{\lambda/D_{\rm a}}}}$$
(B3b)

We can obtain $c_a(r, t)$ either numerically or analytically for large times t. The large-time approximation of Li⁺ concentration on the anode particle surface, before plating occurs, is given by

$$c_{\rm a}(L_{\rm a}, t) = \frac{3I}{L_{\rm a}}t + \frac{IL_{\rm a}}{5D_{\rm a}} + c_{\rm a,0}$$
 (B4)

As charging progresses and the anode electric potential decreases, in eq 3, we have

$$\begin{split} \exp[-0.5(\phi_{a} - \phi_{e} - U_{a}(c_{a}/c_{a,\text{max}})] \\ \gg \exp[0.5(\phi_{a} - \phi_{e} - U_{a}(c_{a}/c_{a,\text{max}})] \end{split} \tag{B5}$$

By solving for the Li-plating overpotential $\eta_{\rm pl}$ from a dimensionless form of eq 3, we obtain

$$\eta_{\rm pl} = -2\ln\left\{\frac{I\exp[-0.5U_{\rm a}(c_{\rm a}/c_{\rm a,max}) - {\rm Ca}]}{k_{\rm a,int}\sqrt{c_{\rm a}(1 - c_{\rm a}/c_{\rm a,max})}}\right\}$$
(B6)

The onset of Li plating is reached when the Li-plating overpotential η_{vl} drops to zero, leading to the condition,

$$\frac{I\exp[-0.5U_{a}(c_{a}/c_{a,\max}) - Ca]}{k_{a,\inf}\sqrt{c_{a}(1 - c_{a}/c_{a,\max})}} = 1$$
(B7)

we combine eqs 6a with p = 0, eqs B7 and B3 to obtain the Liplating onset time, $t_{\rm pl}$,

$$\left(\frac{Ie^{-Ca}}{k_{a,int}\sqrt{c^{\Theta}}}\right)^{2} \frac{1}{c_{a,max}} = f[c_{a}(L_{a}, t_{pl})/c_{a,max}]$$
(B8)

where *f* is a function of the Li⁺ stoichiometry in the anode,

$$f(\xi) = \xi(1 - \xi)e^{U_a(\xi)}$$
(B9)

Therefore, the condition under which no Li plating occurs can be expressed as

$$\left(\frac{Ie^{-Ca}}{k_{a,int}\sqrt{c^{\Theta}}}\right)^{2} \frac{1}{c_{a,max}} < f(\xi_{f})$$
(B10)

where $\xi_f = c_{a,f}/c_{a,max}$ represents the Li⁺ stoichiometry at the anode particle surface at the final charging time t_f .

Similarly, by combining eqs 3, 6a, B2 and B3, we can compute the time at which the anode potential drops to zero, $t_{d_{1} < 0}$,

$$\left(\frac{I}{k_{\text{a,int}}\sqrt{c_{\text{e}}}}\right)^{2} \frac{1}{c_{\text{a,max}}} = f[c_{\text{a}}(L_{\text{a}}, t_{\phi_{\text{a}}<0})/c_{\text{a,max}}]$$
(B11)

and the condition under which the anode electric potential remains positive,

$$\left(\frac{I}{k_{\text{a,int}}\sqrt{c_{\text{e}}}}\right)^{2} \frac{1}{c_{\text{a,max}}} < f(\xi_{\text{f}})$$
(B12)

Here, c_e is the steady-state Li⁺ concentration in the electrolyte given by eq B2 at $x = L_a$. The validity condition for eq B12 is met when the characteristic diffusion time of Li⁺ in the liquid electrolyte is much smaller than the final charging time $t_{\rm fr}$

$$\frac{(L - L_{\rm a})^2}{D_{\rm +}} \ll t_{\rm f} \tag{B13}$$

The condition in eq B13 for eq B12 can be expressed as

$$\xi_{\rm cr} \ll \xi_{\rm f}$$
 (B14)

where

$$\xi_{\rm cr} = \frac{3I(L - L_{\rm a})^2}{D_{+}L_{\rm a}c_{\rm a,max}} + \frac{IL_{\rm a}}{5D_{\rm a}c_{\rm a,max}} + \frac{c_{\rm a,0}}{c_{\rm a,max}}$$
(B15)

if we adopt the large-time approximation for c_{af} given by eq B4.

■ ASSOCIATED CONTENT

5 Supporting Information

The Supporting Information is available free of charge at https://pubs.acs.org/doi/10.1021/acsenergylett.5c00322.

Details of numerical simulations capturing the electric potential and ion concentration profiles, the temporal evolutions of plating overpotential, the parameters used in the simulations, and a summary of the operating conditions and parameters from experimental studies in the literature used for comparison (PDF)

■ AUTHOR INFORMATION

Corresponding Author

Weiyu Li — Department of Mechanical Engineering, University of Wisconsin—Madison, Madison, Wisconsin 53706, United States; ⊙ orcid.org/0000-0002-7857-8115; Email: weiyu.li@wisc.edu

Complete contact information is available at: https://pubs.acs.org/10.1021/acsenergylett.5c00322

Notes

The author declares no competing financial interest.

REFERENCES

- (1) Liu, Y.; Zhu, Y.; Cui, Y. Challenges and opportunities towards fast-charging battery materials. *Nature Energy* **2019**, *4*, 540–550.
- (2) Huang, W.; et al. Onboard early detection and mitigation of lithium plating in fast-charging batteries. *Nat. Commun.* **2022**, *13*, 7091.
- (3) Konz, Z. M.; Wirtz, B. M.; Verma, A.; Huang, T.-Y.; Bergstrom, H. K.; Crafton, M. J.; Brown, D. E.; McShane, E. J.; Colclasure, A. M.; McCloskey, B. D. High-throughput Li plating quantification for fast-charging battery design. *Nature Energy* **2023**, *8*, 450.
- (4) Paul, P. P.; et al. A review of existing and emerging methods for lithium detection and characterization in Li-ion and Li-metal batteries. *Adv. Energy Mater.* **2021**, *11*, 2100372.
- (5) Ma, X.; Harlow, J. E.; Li, J.; Ma, L.; Hall, D. S.; Buteau, S.; Genovese, M.; Cormier, M.; Dahn, J. Hindering rollover failure of Li[Ni_{0.5}Mn_{0.3} Co_{0.2}] O₂/graphite pouch cells during long-term cycling. *J. Electrochem. Soc.* **2019**, *166*, A711–A724.
- (6) Lin, D.; Liu, Y.; Cui, Y. Reviving the lithium metal anode for high-energy batteries. *Nature Nanotechnol.* **2017**, *12*, 194–206.
- (7) Li, W.; Tchelepi, H. A.; Ju, Y.; Tartakovsky, D. M. Stability-guided strategies to mitigate dendritic growth in lithium-metal batteries. *J. Electrochem. Soc.* **2022**, *169*, No. 060536.
- (8) Kazyak, E.; Chen, K.-H.; Chen, Y.; Cho, T. H.; Dasgupta, N. P. Enabling 4C fast charging of lithium-ion batteries by coating graphite with a solid-state electrolyte. *Adv. Energy Mater.* **2022**, *12*, 2102618.
- (9) Tallman, K. R.; Yan, S.; Quilty, C. D.; Abraham, A.; McCarthy, A. H.; Marschilok, A. C.; Takeuchi, K. J.; Takeuchi, E. S.; Bock, D. C. Improved capacity retention of lithium ion batteries under fast charge via metal-coated graphite electrodes. *J. Electrochem. Soc.* **2020**, *167*, 160503.
- (10) Lee, S.-M.; Kim, J.; Moon, J.; Jung, K.-N.; Kim, J. H.; Park, G.-J.; Choi, J.-H.; Rhee, D. Y.; Kim, J.-S.; Lee, J.-W.; Park, M.-S. A cooperative biphasic MoOx—MoPx promoter enables a fast-charging lithium-ion battery. *Nat. Commun.* **2021**, *12*, 39.
- (11) Zhang, S. S. Design aspects of electrolytes for fast charge of Li-ion batteries. *InfoMat* **2021**, *3*, 125–130.
- (12) Yue, X.; Zhang, J.; Dong, Y.; Chen, Y.; Shi, Z.; Xu, X.; Li, X.; Liang, Z. Reversible Li plating on graphite anodes through electrolyte engineering for fast-charging batteries. *Angew. Chem., Int. Ed.* **2023**, *62*, No. e202302285.
- (13) Liu, Y.; Lin, D.; Li, Y.; Chen, G.; Pei, A.; Nix, O.; Li, Y.; Cui, Y. Solubility-mediated sustained release enabling nitrate additive in carbonate electrolytes for stable lithium metal anode. *Nat. Commun.* **2018**, *9*, 3656.
- (14) Liu, Q.; Petibon, R.; Du, C.; Dahn, J. Effects of electrolyte additives and solvents on unwanted lithium plating in lithium-ion cells. *J. Electrochem. Soc.* **2017**, *164*, No. A1173.
- (15) Rangarajan, S. P.; Barsukov, Y.; Mukherjee, P. P. Anode potential controlled charging prevents lithium plating. *Journal of Materials Chemistry A* **2020**, *8*, 13077–13085.
- (16) Pande, V.; Viswanathan, V. Robust high-fidelity DFT study of the lithium-graphite phase diagram. *Physical Review Materials* **2018**, 2, 125401.
- (17) Liang, H.; Wang, L.; He, Y.; Song, Y.; Gao, J.; Xu, G.; Xu, H.; Zhang, H.; He, X. Reversible lithium plating in the pores of a graphite electrode delivers additional capacity for existing lithium-ion batteries enabled by a compatible electrolyte. *Chemical Engineering Journal* **2023**, 454, 140290.
- (18) Fitzhugh, W.; Li, X. Modulation of ionic current limitations by doping graphite anodes. *J. Electrochem. Soc.* **2018**, *165*, A2233.
- (19) Mukherjee, R.; Thomas, A. V.; Datta, D.; Singh, E.; Li, J.; Eksik, O.; Shenoy, V. B.; Koratkar, N. Defect-induced plating of lithium metal within porous graphene networks. *Nat. Commun.* **2014**, *5*, 3710.
- (20) Hayat, K.; Vega, L.; AlHajaj, A. What have we learned by multiscale models on improving the cathode storage capacity of Li-air batteries? Recent advances and remaining challenges. *Renewable and Sustainable Energy Reviews* **2022**, *154*, 111849.
- (21) Ryan, E. M.; Mukherjee, P. P. Mesoscale modeling in electrochemical devices—A critical perspective. *Prog. Energy Combust. Sci.* **2019**, *71*, 118–142.

- (22) Zhang, X.; Tartakovsky, D. M. Effective ion diffusion in charged nanoporous materials. *J. Electrochem. Soc.* **2017**, *164*, E53.
- (23) Arunachalam, H.; Onori, S. Full homogenized macroscale model and pseudo-2-dimensional model for lithium-ion battery dynamics: comparative analysis, experimental verification and sensitivity analysis. *J. Electrochem. Soc.* **2019**, *166*, A1380.
- (24) Boso, F.; Li, W.; Um, K.; Tartakovsky, D. M. Impact of carbon binder domain on the performance of lithium-metal batteries. *J. Electrochem. Soc.* **2022**, *169*, 100550.
- (25) Arora, P.; Doyle, M.; White, R. E. Mathematical modeling of the lithium deposition overcharge reaction in lithium-ion batteries using carbon-based negative electrodes. *J. Electrochem. Soc.* **1999**, *146*, 3543.
- (26) Yang, X.-G.; Leng, Y.; Zhang, G.; Ge, S.; Wang, C.-Y. Modeling of lithium plating induced aging of lithium-ion batteries: Transition from linear to nonlinear aging. *J. Power Sources* **2017**, *360*, 28–40.
- (27) Hein, S.; Danner, T.; Latz, A. An electrochemical model of lithium plating and stripping in lithium ion batteries. *ACS Applied Energy Materials* **2020**, *3*, 8519–8531.
- (28) Hess, M. Temperature-dependence of the solid-electrolyte interphase overpotential: part I. Two parallel mechanisms, one phase transition. *J. Electrochem. Soc.* **2018**, *165*, A323.
- (29) Maraschky, A.; Akolkar, R. Mechanism explaining the onset time of dendritic lithium electrodeposition via considerations of the Li⁺ transport within the solid electrolyte interphase. *J. Electrochem. Soc.* **2018**, *165*, D696.
- (30) Maraschky, A.; Akolkar, R. Temperature dependence of dendritic lithium electrodeposition: a mechanistic study of the role of transport limitations within the SEI. *J. Electrochem. Soc.* **2020**, *167*, No. 062503.
- (31) Smith, R. B.; Bazant, M. Z. Multiphase porous electrode theory. *J. Electrochem. Soc.* **2017**, *164*, E3291.
- (32) Li, Y.; El Gabaly, F.; Ferguson, T. R.; Smith, R. B.; Bartelt, N. C.; Sugar, J. D.; Fenton, K. R.; Cogswell, D. A.; Kilcoyne, A. D.; Tyliszczak, T.; Bazant, M. Z.; Chueh, W. C. Current-induced transition from particle-by-particle to concurrent intercalation in phase-separating battery electrodes. *Nature materials* **2014**, *13*, 1149–1156.
- (33) Hyun, H.; Jeong, K.; Hong, H.; Seo, S.; Koo, B.; Lee, D.; Choi, S.; Jo, S.; Jung, K.; Cho, H.-H.; Han, H. N.; Shin, T. J.; Lim, J. Suppressing high-current-induced phase separation in Ni-rich layered oxides by electrochemically manipulating dynamic lithium distribution. *Adv. Mater.* **2021**, *33*, 2105337.
- (34) Ahn, S.; et al. Chemical origins of a fast-charge performance in disordered carbon anodes. *ACS Applied Energy Materials* **2023**, *6*, 8455–8465.
- (35) Farkhondeh, M.; Pritzker, M.; Fowler, M.; Safari, M.; Delacourt, C. Mesoscopic modeling of Li insertion in phase-separating electrode materials: application to lithium iron phosphate. *Phys. Chem. Chem. Phys.* **2014**, *16*, 22555–22565.
- (36) Gao, T.; Han, Y.; Fraggedakis, D.; Das, S.; Zhou, T.; Yeh, C.-N.; Xu, S.; Chueh, W. C.; Li, J.; Bazant, M. Z. Interplay of lithium intercalation and plating on a single graphite particle. *Joule* **2021**, *5*, 393–414.
- (37) Chen, Y.; Chen, K.-H.; Sanchez, A. J.; Kazyak, E.; Goel, V.; Gorlin, Y.; Christensen, J.; Thornton, K.; Dasgupta, N. P. Operando video microscopy of Li plating and re-intercalation on graphite anodes during fast charging. *Journal of Materials Chemistry A* **2021**, 9, 23522–23536.
- (38) Lain, M. J.; Kendrick, E. Understanding the limitations of lithium ion batteries at high rates. *J. Power Sources* **2021**, 493, 229690.
- (39) Colclasure, A. M.; Dunlop, A. R.; Trask, S. E.; Polzin, B. J.; Jansen, A. N.; Smith, K. Requirements for enabling extreme fast charging of high energy density Li-ion cells while avoiding lithium plating. *J. Electrochem. Soc.* **2019**, *166*, A1412.
- (40) Mao, C.; Ruther, R. E.; Li, J.; Du, Z.; Belharouak, I. Identifying the limiting electrode in lithium ion batteries for extreme fast charging. *Electrochemistry communications* **2018**, *97*, 37–41.
- (41) Yao, K. P.; Okasinski, J. S.; Kalaga, K.; Shkrob, I. A.; Abraham, D. P. Quantifying lithium concentration gradients in the graphite electrode of Li-ion cells using operando energy dispersive X-ray diffraction. *Energy Environ. Sci.* **2019**, *12*, 656–665.

- (42) Ge, H.; Aoki, T.; Ikeda, N.; Suga, S.; Isobe, T.; Li, Z.; Tabuchi, Y.; Zhang, J. Investigating lithium plating in lithium-ion batteries at low temperatures using electrochemical model with NMR assisted parameterization. *J. Electrochem. Soc.* **2017**, *164*, A1050.
- (43) Mei, W.; Zhang, L.; Sun, J.; Wang, Q. Experimental and numerical methods to investigate the overcharge caused lithium plating for lithium ion battery. *Energy storage materials* **2020**, *32*, 91–104.
- (44) Ho, A. S.; Parkinson, D. Y.; Finegan, D. P.; Trask, S. E.; Jansen, A. N.; Tong, W.; Balsara, N. P. 3D detection of lithiation and lithium plating in graphite anodes during fast charging. *ACS Nano* **2021**, *15*, 10480–10487.
- (45) Finegan, D. P.; et al. Spatial dynamics of lithiation and lithium plating during high-rate operation of graphite electrodes. *Energy Environ. Sci.* **2020**, *13*, 2570–2584.
- (46) von Lüders, C.; Keil, J.; Webersberger, M.; Jossen, A. Modeling of lithium plating and lithium stripping in lithium-ion batteries. *J. Power Sources* **2019**, *414*, 41–47.
- (47) Brodsky Ringler, P.; Wise, M.; Ramesh, P.; Kim, J. H.; Canova, M.; Bae, C.; Deng, J.; Park, H. Modeling of lithium plating and stripping dynamics during fast charging. *Batteries* **2023**, *9*, 337.
- (48) Li, Y.; et al. Origin of fast charging in hard carbon anodes. *Nature Energy* **2024**, *9*, 134–142.
- (49) Khoo, E.; Zhao, H.; Bazant, M. Z. Linear stability analysis of transient electrodeposition in charged porous media: Suppression of dendritic growth by surface conduction. *J. Electrochem. Soc.* **2019**, *166*, A2280.
- (50) Li, W.; Tchelepi, H. A.; Tartakovsky, D. M. Screening of Electrolyte-Anode Buffers to Suppress Lithium Dendrite Growth in All-Solid-State Batteries. *J. Electrochem. Soc.* **2023**, *170*, No. 050510.
- (51) Li, W.; Tartakovsky, D. M. Effective representation of active material and carbon binder in porous electrodes. *J. Electrochem. Soc.* **2022**, *169*, No. 040556.
- (52) Yamada, Y.; Wang, J.; Ko, S.; Watanabe, E.; Yamada, A. Advances and issues in developing salt-concentrated battery electrolytes. *Nature Energy* **2019**, *4*, 269–280.
- (53) Girard, G. M.; Hilder, M.; Nucciarone, D.; Whitbread, K.; Zavorine, S.; Moser, M.; Forsyth, M.; MacFarlane, D. R.; Howlett, P. C. Role of Li concentration and the SEI layer in enabling high performance Li metal electrodes using a phosphonium bis (fluorosulfonyl) imide ionic liquid. *J. Phys. Chem. C* **2017**, *121*, 21087–21095.
- (54) Takenaka, N.; Fujie, T.; Bouibes, A.; Yamada, Y.; Yamada, A.; Nagaoka, M. Microscopic formation mechanism of solid electrolyte interphase film in lithium-ion batteries with highly concentrated electrolyte. *J. Phys. Chem. C* **2018**, *122*, 2564–2571.
- (55) Baker, D. R.; Verbrugge, M. W. Intercalate diffusion in multiphase electrode materials and application to lithiated graphite. *J. Electrochem. Soc.* **2012**, *159*, A1341.
- (56) Mastali, M.; Farkhondeh, M.; Farhad, S.; Fraser, R. A.; Fowler, M. Electrochemical modeling of commercial LiFePO4 and graphite electrodes: kinetic and transport properties and their temperature dependence. *J. Electrochem. Soc.* **2016**, *163*, A2803.
- (57) Li, W.; Tartakovsky, D. M. Effective models of heat conduction in composite electrodes. *J. Electrochem. Soc.* **2023**, *170*, 100503.
- (58) Luo, M.; Mijailovic, A. S.; Wang, G.; Wu, Q.; Sheldon, B. W.; Lu, W. Understanding particle size effect on fast-charging behavior of graphite anode using ultra-thin-layer electrodes. *Journal of Energy Storage* **2024**, *104*, 114521.
- (59) Xu, L.; Yang, Y.; Xiao, Y.; Cai, W.-L.; Yao, Y.-X.; Chen, X.-R.; Yan, C.; Yuan, H.; Huang, J.-Q. In-situ determination of onset lithium plating for safe Li-ion batteries. *Journal of Energy Chemistry* **2022**, *67*, 255–262.
- (60) Wandt, J.; Jakes, P.; Granwehr, J.; Eichel, R.-A.; Gasteiger, H. A. Quantitative and time-resolved detection of lithium plating on graphite anodes in lithium ion batteries. *Mater. Today* **2018**, *21*, 231–240.
- (61) McShane, E. J.; Colclasure, A. M.; Brown, D. E.; Konz, Z. M.; Smith, K.; Mc-Closkey, B. D. Quantification of inactive lithium and solid—electrolyte interphase species on graphite electrodes after fast charging. ACS Energy Letters 2020, 5, 2045–2051.

- (62) Uhlmann, C.; Illig, J.; Ender, M.; Schuster, R.; Ivers-Tiffée, E. In situ detection of lithium metal plating on graphite in experimental cells. *J. Power Sources* **2015**, *279*, 428–438.
- (63) Mijailovic, A. S.; Wang, G.; Li, Y.; Yang, J.; Lu, W.; Wu, Q.; Sheldon, B. W. Analytical and numerical analysis of lithium plating onset in single and bilayer graphite electrodes during fast charging. *J. Electrochem. Soc.* **2022**, *169*, No. 060529.